






Original Article


Numerical investigation of hydro-morphodynamic characteristics of a cascading failure of landslide dams


ZHONG Qiming^{1,2,3*}  <https://orcid.org/0000-0001-6077-5252>;  e-mail: qmzhong@nhri.cn

CHEN Lingchun¹  <https://orcid.org/0009-0009-2885-2583>; e-mail: lcchen@nhri.cn

MEI Shengyao¹  <https://orcid.org/0000-0002-0107-4998>; e-mail: symei@nhri.cn

SHAN Yibo¹  <https://orcid.org/0009-0003-9092-5655>; e-mail: ybshan@nhri.cn

WU Hao¹  <https://orcid.org/0000-0002-9380-7369>; e-mail: wuhao@nhri.cn

ZHAO Kunpeng¹  <https://orcid.org/0000-0002-6648-0663>; e-mail: kpzhao@nhri.cn

*Corresponding author

¹ Department of Geotechnical Engineering, Nanjing Hydraulic Research Institute, Nanjing 210024, China

² National Key Laboratory of Water Disaster Prevention, Nanjing 210098, China

³ Key Laboratory of Reservoir and Dam Safety of the Ministry of Water Resources, Nanjing 210029, China

Citation: Zhong QM, Chen LC, Mei SY, et al. (2024) Numerical investigation of hydro-morphodynamic characteristics of a cascading failure of landslide dams. Journal of Mountain Science 21(6). <https://doi.org/10.1007/s11629-023-8411-0>

© Science Press, Institute of Mountain Hazards and Environment, CAS and Springer-Verlag GmbH Germany, part of Springer Nature 2024

Abstract: A cascading failure of landslide dams caused by strong earthquakes or torrential rains in mountainous river valleys can pose great threats to people's lives, properties, and infrastructures. In this study, based on the three-dimensional Reynolds-averaged Navier-Stokes equations (RANS), the renormalization group (RNG) $k-\varepsilon$ turbulence model, suspended and bed load transport equations, and the instability discriminant formula of dam breach side slope, and the explicit finite volume method (FVM), a detailed numerical simulation model for calculating the hydro-morphodynamic characteristics of cascading dam breach process has been developed. The developed numerical model can simulate the breach hydrograph and the dam breach morphology evolution during the cascading failure process of landslide dams. A model test of the breaches of two cascading landslide dams has been used as the validation case. The

comparison of the calculated and measured results indicates that the breach hydrograph and the breach morphology evolution process of the upstream and downstream dams are generally consistent with each other, and the relative errors of the key breaching parameters, i.e., the peak breach flow and the time to peak of each dam, are less than $\pm 5\%$. Further, the comparison of the breach hydrographs of the upstream and downstream dams shows that there is an amplification effect of the breach flood on the cascading landslide dam failures. Three key parameters, i.e., the distance between the upstream and the downstream dams, the river channel slope, and the downstream dam height, have been used to study the flood amplification effect. The parameter sensitivity analyses show that the peak breach flow at the downstream dam decreases with increasing distance between the upstream and the downstream dams, and the downstream dam height. Further, the peak breach flow at the downstream dam first increases and then decreases with steepening of the river channel slope. When the flood caused by the

Received: 24-Oct-2023
1st Revision: 23-Nov-2023
2nd Revision: 08-Feb-2024
3rd Revision: 01-Apr-2024
Accepted: 09-Apr-2024

upstream dam failure flows to the downstream dam, it can produce a surge wave that overtops and erodes the dam crest, resulting in a lowering of the dam crest elevation. This has an impact on the failure occurrence time and the peak breach flow of the downstream dam. The influence of the surge wave on the downstream dam failure process is related to the volume of water that overtops the dam crest and the erosion characteristics of dam material. Moreover, the cascading failure case of the Xiaogangjian and Lower Xiaogangjian landslide dams has also been used as the representative case for validating the model. In comparisons of the calculated and measured breach hydrographs and final breach morphologies, the relative errors of the key dam breaching parameters are all within $\pm 10\%$, which verify the rationality of the model is applicable to real-world cases. Overall, the numerical model developed in this study can provide important technical support for the risk assessment and emergency treatment of failures of cascading landslide dams.

Keywords: Cascading landslide dams; Cascading dam failure process; Detailed numerical simulation model; Flood amplification effect; Parameter sensitivity analyses

1 Introduction

Triggered by earthquakes and rainfalls, landslide dams are one of the common natural disasters in mountainous river valleys (Costa and Schuster 1988; Fan et al. 2020). Comparing with artificial embankment dams, landslide dams have three major characteristics that are different from the embankment dams, i.e., dam configuration, dam material, and hydrodynamic condition (Zhong et al. 2021; Zhou et al. 2022). Firstly, the base of a landslide dam is relatively longer in the longitudinal direction along the blocked river. Its upstream and downstream slope angles are smaller and the dam crest is uneven. Secondly, the material of a landslide dam is not uniform and often has a wide gradation. Thirdly, due to a lack of drainage facilities, most landslide dams fail by overtopping flow shortly after their formation; about 85% of the landslide dams have the longevities of less than one year (Shen et al. 2020). In general, the landslide dams often have relatively small hydraulic gradients due to their configurations. Therefore, landslide dams are not susceptible to seepage failure. The statistics showed that more than 90% landslide dam failures were

induced by overtopping flow (Zhong et al., 2021). It is worth mentioning that clusters of landslide dams may be scattered along mountainous river valleys after large earthquakes (Cui et al. 2009). As such, the cascading landslide dams may collapse like dominoes (Hu et al. 2022). For instance, after the occurrence of Wenchuan earthquake in 2008 in China, 257 landslide dams were formed, resulted in severe flash floods after their failures (Fan et al. 2018).

In recent years, both experimental and numerical studies were conducted on overtopping-induced breach morphology evolutions and their subsequent hydraulic characteristics of cascading landslide dams. Cao et al. (2011), Niu et al. (2012), Zhou et al. (2013, 2015), Chen et al. (2014), Takayama et al. (2021), Zheng et al. (2022), and Hu et al. (2022) conducted a series of model tests that exhibited the cascading failure process of multiple landslide dams and their influencing factors. The research results indicate a general cognition that a considerable larger peak breach flow may occur due to the cascading landslide dam failures as compare to that of a single landslide dam failure. Further, the configuration of landslide dams, physical and mechanical characteristics of dam material, and hydrodynamic conditions in the model tests have also been discussed. These findings give important insights on the breach process of a cluster of landslide dams in a river channel. However, the breaching model tests for cascading landslide dams were scaled and simplified, and there were many limitations in the layout and boundary conditions of the model tests. Therefore, it is difficult to truly reproduce the hydro-morphodynamic characteristics of an actual cascading failure of landslide dams. Therefore, in the risk assessment of cascading landslide dam failures, the numerical simulation method is preferred. It is to ensure that by using a scientific method, the breach hydrograph and the breach evolution process are determined on a reasonable basis.

Recent developments in computational fluid mechanics and sediment transport have helped to develop numerical models that are useful for risk assessment and emergency treatment of landslide dam failures. However, most of them have been developed for a single landslide dam failure, while numerical models specially developed to predict flood hydrographs caused by the cascading failures of multiple landslide dams are relatively rare. Some numerical models for a single landslide dam failure

have been modified and applied to cascading landslide dam failures, which can be classified as simplified and detailed physically-based models, respectively. Modified from a simplified physically-based landslide dam breach model developed by Chang and Zhang (2010), Shi et al. (2015) reproduced the flood hydrograph caused by the cascading breaching of the Tangjiashan landslide dam and two smaller downstream landslide dams in the Tongkou River, China. Thereafter, Zhu et al. (2021) presented the work on risk-based warning decision making on the breaching of the same cascading landslide dams. Based on the simplified physically-based model proposed by Chen et al. (2015), Chen et al. (2018) reviewed a cascading landslide dam failure case caused by the Wenchuan earthquake. Utilizing the two-dimensional shallow water equations and non-equilibrium sediment transport models (i.e., Cao et al. 2004; Guan et al. 2014), Cao et al. (2011) and Yang et al. (2020) developed detailed physically-based models to depict the hydro-morphodynamic process during cascading landslide dam failures.

For a simplified physically-based model, to facilitate the numerical calculations, only regular shapes can be used in the dam configuration and breach morphology during a failure process, and the breach size development and the corresponding flood hydrograph through the breach are estimated using the simplified soil erosion and weir flow equations, respectively. Developed under certain simplifications and assumptions, the simplified physically-based model has the characteristics of considering only the necessary minimum physical processes and high computational efficiency (ASCE/EWRI Task Committee 2011; Zhong et al. 2016). On the other hand, the simplified model has shortcomings in the description of hydrodynamic and morphodynamic processes (Wu et al. 2024).

In order to scientifically and reasonably mimic a cascading failure of landslide dams, detailed physically-based models are preferred, because they can consider the complex terrain and hydro-morphodynamic characteristics during landslide dam breaching. The comparison of the numerical simulation results and model test data showed that the detailed physically-based models calibrated with observed data for a single landslide dam were applicable to cascading failures of landslide dams (Cao et al. 2011; Yang et al. 2020). However, there are only few three-dimensional detailed numerical models

available for simulating cascading dam failures. There is also insufficient research on the factors affecting the amplification effect of cascading dam breach flow.

This study seeks to address the research gaps by developing a detailed numerical model to simulate the hydro-morphodynamic process due to the failure of a cluster of landslide dams in a river valley. In this study, to track the water-sediment interface of free-surface flow, the three-dimensional Reynolds-averaged Navier-Stokes equations (RANS) equations which include the continuity and momentum equations, and the volume of fluid (VOF) method have been integrated to describe the motion of the incompressible fluid. The renormalization group (RNG) k - ϵ turbulence model has been used to describe the hydrodynamic features of the turbulent flow due to landslide dam breaching. The equilibrium suspended and bed load transport equations have been used to depict the erosion and sedimentation processes of landslide deposit under the action of flood flow. An explicit finite volume method (FVM) has been utilized to solve the governing equation, and a numerical simulation method by lowering the higher elevation cell and raising the lower elevation cell based on the soil internal friction angle has been used to simulate the breach side slope instability. The model developed in this study has been verified by the experimental data of two cascading dam failures. Subsequently, considering the cascading dam distribution, the potential energy of the river, and the dams' geometry, three key parameters, i.e., the distance between the upstream and downstream dams, the river channel slope, and the downstream dam height have been selected for the parameter sensitivity analyses of the cascading breach process. The amplification effect of the cascading flood and its influencing factors are discussed comprehensively. Finally, the actual failure case of the Xiaogangjian and Lower Xiaogangjian landslide dams in Mianyuan River has been adopted for validating the applicability of the proposed model to real-world cases.

Comparing with simplified physically-based models and one- and two-dimensional detailed physically-based models, the proposed numerical model in this study offers higher precision, rendering it more suitable for the application. Additionally, the proposed numerical model is not confined to simple hydrodynamic conditions, such as the steady laminar flow. Instead, it utilizes the RNG turbulence model to compute the complex hydrodynamic conditions. These features make the model particularly applicable to the

cascading landslide dam breach scenarios. Furthermore, by incorporating the entrainment and deposition processes of suspended and bed load sediment into the model, and considering the instability of the breach side slope during a dam breach process based on the mass conservation principle, the model can scientifically consider the soil erosion process and breach morphology evolution during dam breaching. This enhancement enables the proposed numerical model with advantages in simulating breach hydrograph and landscape evolution.

2 Methods

In the numerical model developed in this study, the calculation process of the numerical modeling of a cascading failure of landslide dams is divided into four steps. Firstly, for the upper landslide dam breaching, using the clear water condition in the dammed lake, and the suspended and bed load transport equations, the sediment concentration of the flood flow at the outlet of the breach is obtained. Secondly, using the obtained sediment concentration in the breach flow for the flood routing, in which the morphological evolution of a river channel due to the entrainment and deposition is calculated. Thirdly, based on the relationship between the water level and the dammed lake storage, and considering the sediment-carrying inflow, the water level rising process, and the hydro-morphodynamic process of the downstream landslide dam breaching are calculated. Fourthly, calculate the breach flood routing and the failure of the next cascading dam up to the computational boundary.

The highlights of the numerical simulation of an overtopping-induced cascading failure of landslide dams are exhibited in two aspects: (1) the simulation of turbulent flow during a single landslide dam breaching and sediment-carrying flood routing, and (2) the geomorphic evolution due to soil erosion and sedimentation after cascading landslide dam breaching.

In this section, a detailed physically-based hydro-morphodynamic model is described which can predict the cascading landslide dam breaching process. Based on the functionality of each equation, the numerical model is composed of three parts, i.e., fluid motion, soil erosion, and geomorphic evolution. In addition, an explicit FVM based numerical simulation method has been chosen to solve the governing equations of the proposed model.

2.1 Fluid motion

In order to track the free surface of water and sediment, the ratio of the fluid volume to the unit volume (V_F) is introduced to the continuity and momentum equations of the three-dimensional RANS equations.

The continuity equation can be expressed as (Movahedi et al. 2018; Mei et al. 2022):

$$\frac{\partial \rho_w}{\partial t} V_F + \frac{\partial}{\partial x} \rho_w u A_x + \frac{\partial}{\partial y} \rho_w v A_y + \frac{\partial}{\partial z} \rho_w w A_z = 0 \quad (1)$$

where ρ_w is the water density; t is time; the flow velocity component of u , v , and w are in x , y , and z directions, respectively; V_F follows $\partial V_F / \partial t + \nabla \cdot (u V_F) = 0$; and the flow passing areas of A_x , A_y , and A_z are in x , y , and z directions, respectively.

The momentum equations can be expressed as (Movahedi et al., 2018; Mei et al., 2022):

$$\begin{cases} \frac{\partial u}{\partial t} + \frac{1}{V_F} (u A_x \frac{\partial u}{\partial x} + v A_y \frac{\partial u}{\partial y} + w A_z \frac{\partial u}{\partial z}) = -\frac{1}{\rho_w} \frac{\partial P}{\partial x} + G_x + f_x \\ \frac{\partial v}{\partial t} + \frac{1}{V_F} (u A_x \frac{\partial v}{\partial x} + v A_y \frac{\partial v}{\partial y} + w A_z \frac{\partial v}{\partial z}) = -\frac{1}{\rho_w} \frac{\partial P}{\partial y} + G_y + f_y \\ \frac{\partial w}{\partial t} + \frac{1}{V_F} (u A_x \frac{\partial w}{\partial x} + v A_y \frac{\partial w}{\partial y} + w A_z \frac{\partial w}{\partial z}) = -\frac{1}{\rho_w} \frac{\partial P}{\partial z} + G_z + f_z \end{cases} \quad (2)$$

where P is the intensity of pressure; the mass accelerations of G_x , G_y , and G_z are in x , y , and z directions, respectively; and the viscosity accelerations of f_x , f_y , and f_z are in x , y , and z directions, respectively.

In Eq. (2), f_x , f_y , and f_z can be expressed as:

$$f_i = \frac{\tau_{b,i} \frac{\partial (A_j S_{ij})}{\partial x_j}}{V_F} \quad (3)$$

where f_i is the tensor form of viscosity acceleration, and i can be x or y or z direction; $\tau_{b,i}$ is the tensor form of bed shear stress; S_{ij} is the tensor form of strain rate, which has the following expression:

$$S_{ij} = -(\mu + \mu_t) \left(\frac{\partial u_i}{\partial x_j} + \frac{\partial u_j}{\partial x_i} \right) \quad (4)$$

where μ is the turbulent viscosity coefficient, and μ_t is the dynamic turbulence viscosity coefficient.

During a landslide dam breaching, the hydrodynamic process exhibits complex characteristics due to violent variation of streamflow regime. However, since the standard $k-\varepsilon$ turbulence model assumes that the Reynolds stress and the change in the time-averaged rate are linear and isotropic, it cannot be used to solve the fluid motion with high flow shear force and zigzag streamline. To solve the RANS equations, and improve the computational efficiency and accuracy of turbulent flow, the RNG $k-\varepsilon$ turbulence model, which can

improve the accuracy of the equations and consider the complex rotating flows, has been used to simulate the nonlinear term of Reynolds stress and the change in the time-averaged rate (Yakhot et al. 1992):

$$\frac{\partial(\rho_w k)}{\partial t} + \frac{\partial(\rho_w k u_i)}{\partial x_i} = \frac{\partial}{\partial x_j} \left[\left(\mu + \frac{\mu_t}{\sigma_k} \right) \frac{\partial k}{\partial x_j} \right] + G_k - \rho_w \varepsilon \quad (5)$$

$$\frac{\partial(\rho_w \varepsilon)}{\partial t} + \frac{\partial(\rho_w \varepsilon u_i)}{\partial x_i} = \frac{\partial}{\partial x_j} \left[\left(\mu + \frac{\mu_t}{\sigma_\varepsilon} \right) \frac{\partial \varepsilon}{\partial x_j} \right] + C_1 G_k \frac{\varepsilon}{k} - C_2 \rho_w \frac{\varepsilon^2}{k} \quad (6)$$

where k is the turbulent kinetic energy; ε is the turbulence dissipation rate; u_i is the tensor form of flow velocity; and G_k is the turbulent kinetic energy generated from the velocity gradients; herein, $\mu_t = 0.085k^2/\varepsilon$, $C_1 = 1.42$, $C_2 = 1.68$, and $\sigma_k = \sigma_\varepsilon = 0.7194$.

2.2 Soil erosion

During a cascading failure of landslide dams, the variation of flow velocity leads to a change in fluid density and viscosity coefficient due to the different sediment concentrations in the fluid, thereby affecting the erosion process. In general, the transport modes of landslide deposits can vary between bed load and suspended load (Guan et al. 2014) (Fig. 1). When the flow rate is smaller than the deposition rate of the particle, the suspended load will become bed load; hence, the entrainment and deposition can be regarded as two opposite micro-processes that occur under different hydrodynamic conditions. The suspended load usually has a relatively low concentration and can be transported by the fluid flow (Mei et al. 2022). Because of the limitation of neighboring particles, the bed-material load is often not easy to displace, and the accumulated particles can move in the form of bed load by rolling, saltating, sliding, or drawing along the bed (Samma et al. 2020).

From a microscopic view, the hydrodynamic force around a single soil particle and the boundary layer at the water-soil interface can be calculated in accordance with the erosion mechanism, but there are huge practical difficulties in the corresponding numerical simulation. Therefore, the soil erosion process is commonly calculated using statistically-based empirical models from a macroscopic view.

Up to now, large number of empirical or semi-empirical models have been developed, which can be used to calculate the bed load transport rate. Based on experimental results, empirical formulas usually use the isolated factor method to develop bed load transport rate formulas (i.e., Meyer-Peter and Muller

1948). Based on physical assumptions, semi-empirical models generally determine the basic structure of bed load transport rate formulas, whereas some parameters in the models need to be calibrated utilizing measured experimental data (i.e., Bagnold 1966). However, significant discrepancies may exist among these empirical and semi-empirical models when they are applied in engineering practice. The comparison of five bed load transport rate models (i.e., Meyer-Peter and Muller 1948; Bagnold 1966; Engelund and Fredsoe 1976; Van Rijn 1984; Nielsen, 1992) with experimental data from multiple sources (Meyer-Peter and Muller 1948; Chien and Wan 1999; Roseberry et al. 2012) conducted by Mei et al. (2022) showed that among the five bed load transport rate models, the Meyer-Peter and Muller model was the most accurate. The Meyer-Peter and Muller model has the following expression:

$$q_{b,i} = K(\theta_i - \theta_{cr,i}')^{1.5} \left[g \left(\frac{\rho_{s,i} - \rho_w}{\rho_w} \right) d_i^3 \right]^{0.5} \quad (7)$$

where $q_{b,i}$ is the volumetric bed load transport rate per unit width; K is the bed load coefficient; θ_i is the Shields parameter for soil species i , and $\theta_i = \tau_b/[gd_{50}(\rho_s - \rho_w)]$, in which, τ_b is the bed shear stress, d_i is the mean grain size, $\rho_{s,i}$ is the soil density; g is gravitational acceleration; and $\theta_{cr,i}'$ is the modified dimensionless critical Shields parameter.

Different from the sediment transport in a river channel, landslide dam breach morphology evolution is also affected by the repose angle that accounts for the breach side slope stability supported by the packed soil. Therefore, the modified dimensionless critical Shields parameter is expressed as follows (Soulsby 1997).

$$\theta_{cr,i}' = \theta_{cr,i} \frac{\cos \psi \sin \beta + \sqrt{\cos^2 \beta \tan^2 \varphi_i - \sin^2 \psi \sin^2 \beta}}{\tan \varphi_i} \quad (8)$$

in which

$$\theta_{cr,i} = \frac{0.3}{1 + 1.2d_{*,i}} + 0.055[1 - e^{-0.02d_{*,i}}] \quad (9)$$

where $\theta_{cr,i}$ is the dimensionless critical Shields parameter; ψ is the angle between the water flow and the upstream slope; β is the bed slope angle; φ_i is the internal friction angle of the soil species i ; $d_{*,i}$ is the dimensionless grain size parameter, and $d_{*,i} = d_i[\rho_w(\rho_s - \rho_w)g/\mu^2]^{1/3}$.

The bed load layer thickness needs to be calculated in order to determine the boundary of the bed load and bed-material load; herein, the bed load transport rate is converted into bed load velocity (Van Rijn 1984), as follows:

$$\frac{\delta_{b,i}}{d_i} = 0.3d_*^{0.7} \left(\frac{\theta_i}{\theta_{cr,i}} - 1 \right)^{0.5} \quad (10)$$

$$u_{bedload,i} = \frac{q_{b,i}}{\delta_{b,i}c_{b,i}f_b} \quad (11)$$

where $\delta_{b,i}$ is the bed load layer thickness; $u_{bedload,i}$ is the bed load velocity for soil species i ; $c_{b,i}$ is the volume fraction of soil species i ; and f_b is the critical packing fraction of soil.

For entrainment, the amount of packed soil converted to suspended load can be calculated as follows (Mastbergen and Berg 2003):

$$E_i = \alpha_i n_s d_*^{0.3} (\theta_i - \theta_{cr,i})^{1.5} \left[g \left(\frac{\rho_s - \rho_w}{\rho_w} \right) d_i \right]^{0.5} \quad (12)$$

where E_i is the upward entrainment velocity for soil species i ; α_i is the entrainment rate coefficient for soil species i ; and n_s is the normal direction vector for packed bed interface.

For deposition, the soil deposition velocity of suspended load can be defined as the product of the effective settling velocity and the suspended sediment concentration in the near bed.

$$D_i = \omega_i c_i \quad (13)$$

where D_i is the downward deposition velocity for soil species i ; ω is the settling velocity for soil species i , and $\omega = \nu_t [(10.36^2 + 1.049d_*^3)^{0.5} - 10.36] / d_i$, in which ν_t is the kinematic viscosity of fluid; and c_i is the near bed suspended sediment concentration of soil species i (Soulsby 1997).

For each soil species, the suspended sediment mass concentration can be expressed utilizing the advection-diffusion equation (Samma et al. 2020), as follows:

$$\frac{\partial C_{s,i}}{\partial t} + \nabla \cdot (u_{s,i} C_{s,i}) = \nabla \cdot (\xi C_{s,i}) \quad (14)$$

where $C_{s,i}$ is the suspended sediment mass concentration of soil species i , which is defined as the sediment mass per volume of the fluid-sediment mixture; ξ is the direction diffusion coefficient; $u_{s,i}$ is the suspended sediment velocity, and $u_{s,i} = u_m + \omega C_{s,i}$, in which, u_m is the fluid-sediment mixture velocity, and $c_{s,i}$ is the suspended sediment volume concentration.

2.3 Geomorphic evolution

During the cascading failure of landslide dams due to overtopping breaching, the processes of entrainment and deposition occur simultaneously. As shown in Fig. 1, the geomorphic evolution in the packed bed can be updated based on the calculations of the fluid motion and soil erosion. The upward

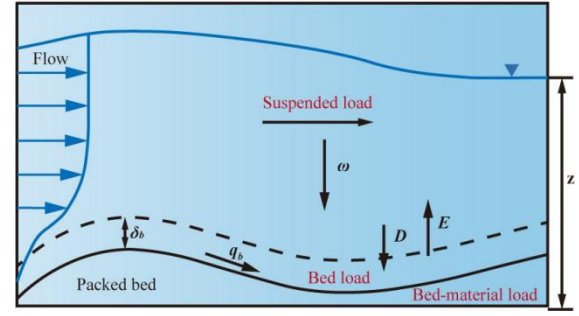


Fig. 1 Schematic diagram of the entrainment and deposition during soil erosion.

entrainment and downward deposition can be calculated by the conservation law of soil mass, as follows:

$$\phi \frac{\partial z}{\partial t} = \left(\frac{\partial q_{bx}}{\partial x} + \frac{\partial q_{by}}{\partial y} + D - E \right) \quad (15)$$

where z is the elevation of the breach bottom; ϕ is the maximum packing fraction, and ϕ can be set as 0.64 (Mei et al. 2022); q_{bx} , q_{by} , D , E are represented as the weighted averages of $q_{bx,i}$, $q_{by,i}$, D_i , E_i based on the soil content.

As the elevation of a breach bottom becomes lower, the breach side slope angle of certain parts of the breach cross section may exceed the critical slope angle. In this case, the breach section becomes unstable. The breach side slope angle will then change and become nearly equal to the internal friction angle by lowering the higher elevation part of the breach section and raising the lower elevation part of the breach section (Guan et al. 2014).

To simulate the sliding process of a breach side slope, the mass conservation of dam material is followed. Firstly, a central grid is selected, and compares with the adjacent grids one by one to judge whether the central grid and the corresponding adjacent grids meet the sliding conditions. Secondly, the minimum sliding height that meets the termination of the sliding process is determined through iterative calculations. The sliding height of each grid as the central grid and the ascending heights of the adjacent grids are determined, and the elevations of all the grids are updated. Thirdly, when all the central grids have no adjacent grids that meet the sliding conditions, the iterative calculations stop, and the breach slide slope is considered stable. The sliding process can be described as follows (Fig. 2) (Guan et al. 2014; Mei et al. 2023).

$$\begin{cases} z_{i+1}' = z_{i+1} - \Delta z \\ z_i' = z_i + \Delta z \end{cases} \quad (16)$$

where z_i' and z_{i+1}' are the bottom elevations of the i th

and $(i+1)$ th cells after sliding, respectively; z_i and z_{i+1} are the bottom elevations of the i th and $(i+1)$ th cells before sliding, respectively; Δz is the variation of the bottom elevation caused by sliding, and $\Delta z = \Delta L(\tan\beta - \tan\phi)/2$, in which, ΔL is the distance between two adjacent cells.

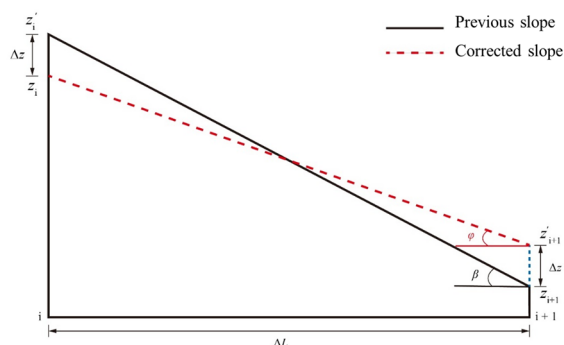


Fig. 2 Schematic diagram of bottom elevation variation of two adjacent cells due to sliding.

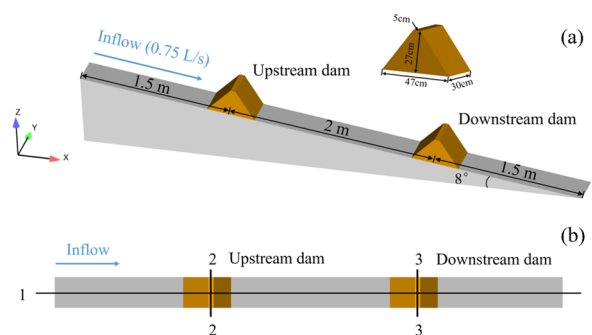


Fig. 3 3D computational model and monitoring sections: (a) Model layout in the numerical modeling; (b) Monitoring sections in longitudinal of cross profiles (top view).

Table 1 Input parameters and their values in the numerical model

Input parameter	Value
Flume length (m)	5
Flume width (m)	0.3
Bottom width of model dam (cm)	47
Top width of model dam (cm)	5
Slope angle of flume (°)	8
Height of model dam (cm)	27
Slope ratio (Vertical/Horizontal)	9:7
Distance between two dams (m)	2

2.4 Numerical simulation method

The continuity and momentum equations of the three-dimensional RANS equations are solved utilizing an explicit FVM on structured staggered grids. The calculated region is subdivided into a mesh with fixed

rectangular cells, and all the calculated variables are set at the center of each cell except for the flow velocities, which are located at cell-faces. To avoid instability in the numerical simulations, the calculation time step and the mesh size are set at a reasonable step and size with due consideration of the soil erosion process, thereby ensuring the soil transportation does not cross multiple computing cells in one time step. The Euler model based VOF method which can accurately describe the interface between water and soil is used to trace the free surface flow by the ratio of the fluid volume to the unit volume (Hirt and Nichols 1981; Marsooli and Wu 2015). Combining with FAVOR (fractional area/volume ratio) method, the geometric features of a complex solid can be analyzed accurately (Liang et al. 2019). That is, when the ratio of the fluid volume to the unit volume is less than 0.35 in a computational grid, it is considered that the grid is full of sediment; otherwise, the grid is considered to contain all water. In addition, due to its advantages of fast convergence and high computational accuracy, generalized minimal residual method is used to solve the algebraic equations (Samma et al. 2020).

3 Validation and Results

3.1 Model set-up and input parameters

In order to verify the detailed numerical model developed in this study, a flume model of a two-cascading landslide dam breaching was conducted by Hu et al. (2022). The results of the model test have been used as a benchmark to study in detail the evolution of the breach hydrograph and breach morphology. The upstream and downstream dams are identical in morphology, and the distances between the inflow boundary and the upstream and downstream dams are 1.5 m and 3.5 m, respectively (Fig. 3a). The input parameters and their values in the numerical model are shown in Table 1.

The grain size distribution curve of the dam material used in the simulation is illustrated in Fig. 4. To simulate the soil properties of the dam material accurately, two particle sizes were selected to mimic the fine and the coarse particles respectively, of which 17% were fine particles and 83% were coarse particles. Kumari et al. (2019) have conducted sensitivity analyses on the critical Shields number, entrainment

Table 2 Basic physical and mechanical parameters of dam materials

Input parameter	Value	
	Fine particles	Coarse particles
d_{50} (mm)	0.45	3.50
ρ_s (kg/m ³)	2650	2650
θ_{cr}	0.15	0.20
α	0.02	0.02
K	7	7
φ (°)	65	65
Percentage (%)	17	83

Note: d_{50} , the mean grain size; ρ_s , Soil density; θ_{cr} , dimensionless critical Shields parameter; α , the entrainment rate coefficient; K is the bed load coefficient; φ , the internal friction angle.

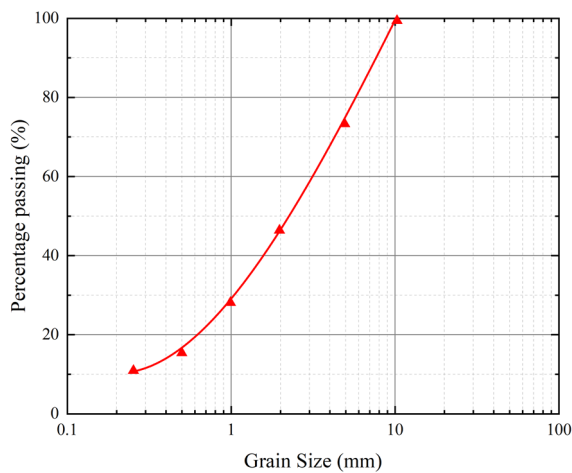


Fig. 4 Grain size distribution of the dam material.

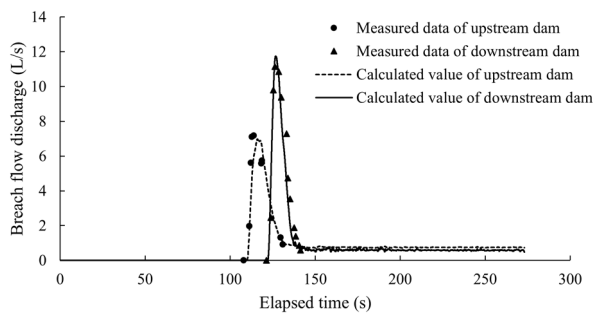


Fig. 5 Comparisons of measured and calculated breach hydrographs at the upstream and downstream dams.

coefficient, and bed load transport coefficient to determine the optimal range of the coefficients. According to the results of their analyses, the values for the basic physical and mechanical parameters of the dam material have been selected, which are shown in Table 2. To achieve accurate simulation results, the dam body size, particle size, and the boundary conditions in the numerical modeling are the same as in the physical model test. Herein, the upper boundary

of the model has been set as the flow boundary, and the inflow is 0.75 L/s, which is a constant inflow in the numerical simulation. The lower boundary has been set as a free flow boundary, and the two sides of the flume have been set as rigid bodies with non-slip boundaries.

Throughout the simulation workflow, the reliance of computational outcomes on grid granularity constitutes a pivotal element of consideration. A diminutive mesh scale predisposes the numerical operations to divergence, which compromises the stability of the system. Conversely, an excessively coarse grid fails to capture the intricacies of topographical features within the three-dimensional representation, thereby undermining the fidelity with which erosion and deposition dynamics associated with mass wasting phenomena are modeled. The extent to which the simulation results are contingent upon mesh size is modulated by an array of parameters, encompassing the dimensions of the particulates constituting the dam material, the spatial extent of the computational domain, and the prevailing hydraulic conditions. In pursuit of balance between computational expediency and precision, whilst concurrently safeguarding the stability of the numerical procedure, the model has been discretized employing structured grids, with each grid dimensioned at 1 cm by 1 cm. To compare the calculated results with the measured data, three monitoring sections in the longitudinal profile (Section 1-1) and cross profile (Section 2-2 and Section 3-3) have been set at the upstream and the downstream dam axes to obtain the calculated breach hydrograph and breach morphology evolution during the cascading landslide dam breach process (Fig. 3b).

3.2 Breach hydrograph

The numerical simulation results show that 110 s after the flume was filled, the water overtopped the upstream dam crest, and the peak breach flow reached 7.0 L/s at 116.0 s after filling. The breach flow overtopped the downstream dam crest at 121 s after the flume was filled, and the peak breach flow reached 11.7 L/s at 126.7 s after filling, which is 1.7 times larger than that of the upstream dam.

Fig. 5 shows the comparisons of measured and calculated breach hydrographs at the upstream dam (Section 2-2) and the downstream dam (Section 3-3). The relative errors of the key breaching parameters of

the measured and calculated results are listed in Table 3. The numerical model has done well to reproduce the cascading dam breach process of the model test. The relative errors of the peak breach flow and the time to peak of each dam are less than $\pm 5\%$, and the amplification effect of cascading flood is also confirmed.

3.3 Breach morphology evolution in longitudinal profile

To verify the rationality of the numerical model in the calculation of breach morphology evolution process in the longitudinal profile, the calculated results of Section 1-1 have been used, and the cascading landslide dam breach process has been comprehensively analyzed according to the dam-break flood characteristics and breach development.

Based on the numerical simulation results, the dam breach process of a single landslide dam can be divided into four stages, i.e., surface erosion, backward erosion, erosion along the flow channel, and breach stabilization. For the upstream dam, in Stage I (Figs. 6a and 6b), the water flow overtops the dam crest 110 s after the filling of the flume, and then the surface erosion occurs on the downstream slope of the dam due to the overtopping flow, while the erosion mainly

occurs at the toe of the downstream dam because of the potential energy of water flow is converted into kinetic energy. In Stage II (Fig. 6c), the overtopping flow retrogressively erodes the downstream slope of the upstream dam, and the backward erosion occurs gradually until the head-cut migrates to the upstream reservoir. During this stage, the river channel between the upstream and downstream dams begins to store water. In Stage III (Fig. 6d), with the increase in the water head of the overtopping flow, the flow shear stress increases, and the breach downcuts rapidly, resulting in a lowering of the dam crest elevation. Meanwhile, accompanied by the lateral expansion of the breach, the breach flow discharge also increases correspondingly to the maximum. During this stage, the water level between the upstream and downstream dams begins to rise rapidly, and the water flow exhibits turbulent characteristics. In Stage IV (Figs. 6e - 6h), with the rapid downcutting and widening of the breach, the upstream water level drops rapidly, and the inflow and outflow of the breach reaches a balance, and the development of the breach stops at 126 s after the filling. As for the downstream dam, similar four stages are also experienced (Figs. 6e - 6h). The start time and end time of the overtopping failure are 121 s and 150 s after the filling, respectively. The comparison of the measured and calculated results indicates that the

Table 3 Comparison of measured and calculated key breaching parameters

Dam name	Parameter	Measured data	Calculated data	Relative error (%)
Upstream dam	Peak breach flow (L/s)	7.2	7.0	-2.8
	Time to peak (s)	113.9	116.0	1.8
Downstream dam	Breach time (s)	126.0	126.0	0
	Peak breach flow (L/s)	11.2	11.7	4.5
	Time to peak (s)	126.4	126.8	0.3

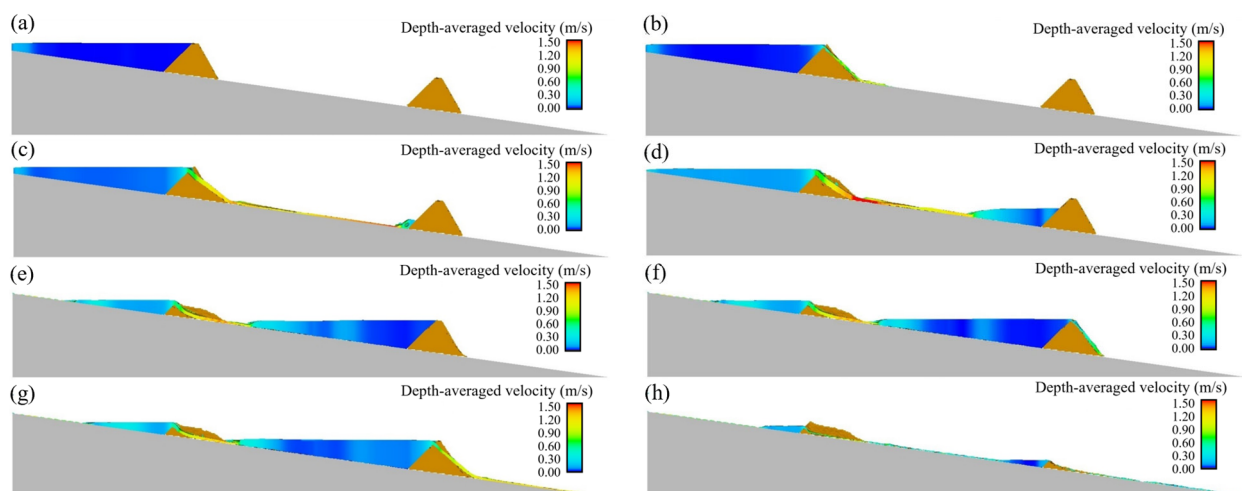


Fig. 6 Variation of calculated depth averaged velocity of the cascading flood in Section 1-1: (a) $t = 110$ s, (b) $t = 111.5$ s, (c) $t = 113$ s, (d) $t = 116$ s, (e) $t = 122$ s, (f) $t = 123$ s, (g) $t = 124$ s, (h) $t = 150$ s.

failure characteristics of the downstream dam are basically the same as that of the upstream dam, but the speed of failure is faster, and the peak breach flow is also significantly higher (Fig. 6), showing the amplification effect. The calculated results in Fig. 6 indicate that the detailed numerical model developed in this study can accurately reproduce the breach morphology evolution process in the longitudinal profile and the characteristics of the outburst flood in the two-cascading landslide dam breach model test.

3.4 Breach morphology evolution in cross profile

Fig. 7 shows the breach morphologies at different times obtained by the numerical simulation and the physical model test (Hu et al. 2022). It shows the breach morphologies at 110 s when the water flow begins to overtop the upstream dam, 121 s when the water flow begins to overtop the downstream dam, and 130 s. The comparisons of the simulated and measured breach morphologies show that the calculated breach morphology is basically consistent with the test results.

Furthermore, Fig. 8 shows the calculated breach

morphology evolution processes in Sections 2-2 and 3-3. When the upstream dam begins to fail, the inflow is smaller than the breach flow, so the water head of the overtopping flow becomes smaller, resulting in the downcutting erosion mainly concentrates in the middle of the dam axis, and the erosion on both sides of the dam body is relatively less. As for the downstream dam, due to the large inflow after the failure of the upstream dam, the overflow shows the characteristics of a full cross-section overtopping, and the overall elevation of the breach bottom becomes lower rapidly. Moreover, the residual dam material of the downstream dam is significantly less than that of the upstream dam when the cascading breach process ends.

4 Discussion and Application

4.1 Discussion of flood amplification effect due to cascading dam failure

Considering the avoidance of complicated terrain conditions and the variation of the multiple input parameters, which affect the analysis results during

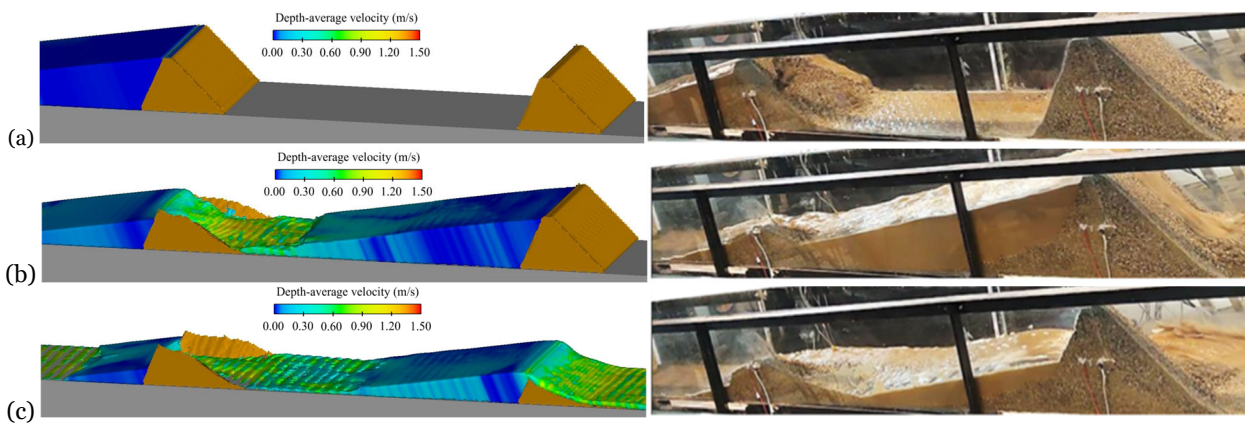


Fig. 7 Comparison of calculated and measured breach morphologies: (a) $t = 110$ s, (b) $t = 121$ s, (c) $t = 130$ s.

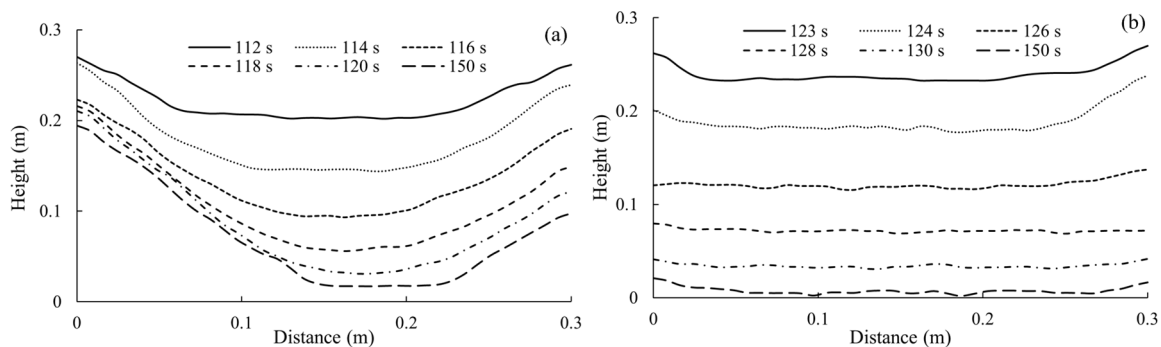


Fig. 8 Calculated breach morphology evolution processes in (a) Section 2-2, (b) Section 3-3.

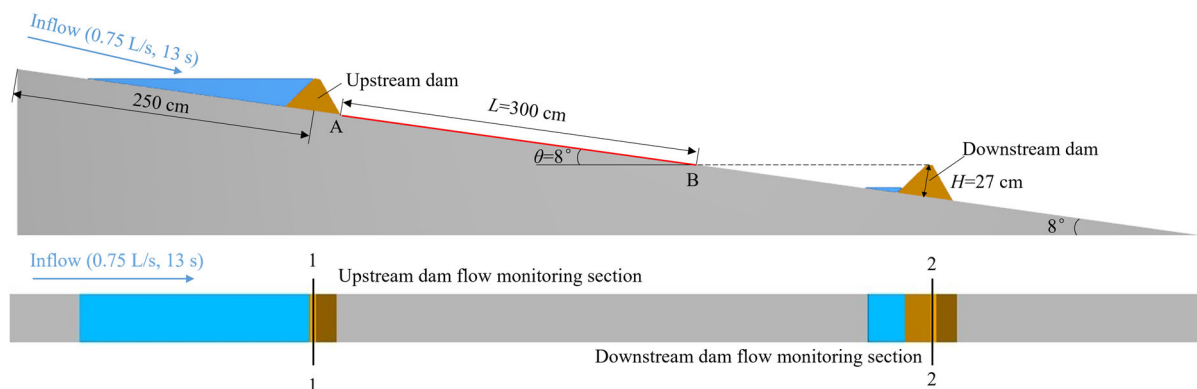


Fig. 9 Boundary conditions for the numerical parametric study.

numerical simulation, the results of the two-cascading landslide dam failure model test with relatively simple boundary conditions conducted by Hu et al. (2022) are used again. Herein, three key parameters, i.e., the distance between the upstream and downstream dams, the river channel slope, and the downstream dam height, have been used to conduct the parameter sensitivity analyses. Based on the calculated results of the numerical model developed in this study, the flood amplification effect and its influencing factors are analyzed thoroughly.

4.1.1 Parameter sensitivity analysis schemes

Because the parameter sensitivity analyses involve the cascading failures of both the upstream and downstream dams, factors such as boundary conditions should be fully taken into account when studying the amplification effect of cascading flood. In order to ensure the rationality of the numerical simulation results, the boundary conditions have been reset.

Fig. 9 shows the setting of the boundary conditions in the parameter sensitivity analyses. In the analyses, it is crucial to ensure that there is only one variable. Since the magnitude of water storage capacity affects the breach flow discharge and breach morphology evolution during dam breaching, it is necessary to maintain the same volume of water during the cascading failure of upstream and downstream dams in the sensitivity analyses. To maintain the water balance during the cascading failure simulation, the inflow has been set to 0.75 L/s, and the inflow duration has been set to 13 s, so the inflow process stops before the complete failure of the upstream dam. The upstream dam configuration is consistent with that in the model test described in Section 3.1, while the distance from the bottom center of the upstream dam

to the inflow boundary has been adjusted to 250 cm. Based on the trial calculations, the residual dam height after the failure of the upstream dam is 4.7 cm, so the initial water depth in front of the downstream dam has been set to the same value as a supplement to ensure the water balance during the cascading failure.

In the sensitivity analysis of the distance between the upstream and downstream dams, the distance between the toe of the downstream slope of the upstream dam (Point A) and the position (Point B) which has the same elevation as the downstream dam crest has been set to 200 cm, 300 cm, and 400 cm, while the other parameters remain unchanged. In the sensitivity analysis of the river channel slope, in order to ensure the storage capacity of the upstream dam does not change, the river channel slope only changes in line AB, which has been set to 3°, 8°, and 13°. In the sensitivity analysis of the downstream dam height, the downstream dam height has been set to 21 cm, 27 cm, and 29 cm, while the upstream and downstream slope ratios of the downstream dam remain unchanged. In the sensitivity analysis of each input parameter, the initial water level has been set to 1 cm below the upstream dam crest, and the schemes for the parameter sensitivity analyses are shown in Table 4.

Table 4 Schemes for parameter sensitivity analyses

No.	Distance of AB (cm)	River channel slope (°)	Downstream dam height (cm)
Control group	300	8	27
Scheme 1	200	8	27
Scheme 2	400	8	27
Scheme 3	300	3	27
Scheme 4		13	
Scheme 5	300	8	21
Scheme 6		8	29

4.1.2 Analysis of calculated results

The calculated results of the control group and each scheme are shown in Table 5. As the inflow boundary conditions and the upstream dam parameters of each scheme are consistent, the breach process of the upstream dam is the same, i.e., the overtopping process originates 3.7 s after the filling, and the time to peak occurs 12.4 s after the filling, with the peak breach flow of 7.2 L/s. In the control group, the dam-break flow overtops the downstream dam 20 s after the filling, and the peak breach flow occurs 26.7 s after the filling, with the value of 9.8 L/s, and the amplification coefficient of the peak breach flow is therefore 1.36.

Schemes 1 and 2 reflect the influence of the distance between the upstream and downstream dams on the cascading failure process, and the breach hydrographs are shown in Fig. 10a. In Scheme 1, the distance between the upstream and downstream dams is the shortest, hence, the overtopping failure occurs firstly due to the shortest duration of flood routing. In Scheme 2, the potential energy difference between the upstream and downstream dams is relatively large when the river slope remains the same, so the surge wave formed by the upstream dam-break flow has more kinetic energy when it moves to the downstream dam. At 17.1 s after the filling, the surge wave overtops the downstream dam crest, resulting in the erosion of the dam crest and the downstream slope, with a maximum reduction of 1.7 cm in the dam height. Therefore, the occurrence of overtopping failure of the downstream dam in Scheme 2 is earlier than that of the control group. From the point of view of peak breach flow, the shorter the distance between the upstream and downstream dams, both the peak breach flow of the downstream dam, and the flood amplification effect are larger.

Schemes 3 and 4 reflect the influence of the river channel slope on the cascading failure process, and the breach hydrographs are shown in Fig. 10b. The calculated results show that the smaller the river

channel slope, the earlier the flow overtops the downstream dam. With the increase in the river channel slope, the peak breach flow increases first and then decreases. The reason is that with the same channel length, the larger the slope ratio, the larger the potential energy between upstream and downstream, and the larger the flood amplification effect. However, for Scheme 4, due to the transition at Point B of the river channel, the momentum of the dam-break flow attenuates here, resulting in a smaller peak breach flow than that of the control group.

Schemes 5 and 6 reflect the influence of the downstream dam height on the cascading failure process, and the breach hydrographs are shown in Fig. 10c. The calculated results show that the lower the downstream dam height, the earlier the flow overtops the downstream dam, the larger the peak breach flow at the downstream dam, and the larger the flood amplification effect. It is worth mentioning that due to the small downstream dam height in Scheme 5, before the water level reaches the downstream dam crest, the surge wave formed by the upstream dam-break flow overtops the downstream dam crest, resulting in an initial notch with a maximum depth of 4 cm in the dam crest, which impacts the downstream dam breach process.

4.1.3 Improved understandings based on numerical modeling

The flood amplification effect due to cascading dam failures has been revealed by a series of previous model tests. However, there are only limited quantitative analyses on the flood amplification effect and its influencing factors. Improved understandings of the cascading failure of landslide dams have been achieved based on the three-dimensional numerical modeling of the two-cascading landslide dam failure model test and sensitivity analyses of the three key parameters. Firstly, surge wave is one of the important phenomena which always occurs during a cascading landslide dam breaching, but it is a difficult phenomenon to model in the numerical modeling.

Table 5 Results of parameter sensitivity analyses

No.	Downstream dam failure time (s)	Time to peak of downstream dam (s)	Peak breach flow of downstream dam (L/s)	Amplification coefficient of breach flow
Control group	20.0	26.7	9.8	1.36
Scheme 1	16.5	23.2	10.3	1.43
Scheme 2	18.1	26.6	7.9	1.10
Scheme 3	19.0	26.6	7.4	1.03
Scheme 4	21.9	29.4	8.9	1.24
Scheme 5	13.1	19.3	10.8	1.50
Scheme 6	29.7	34.2	8.2	1.14

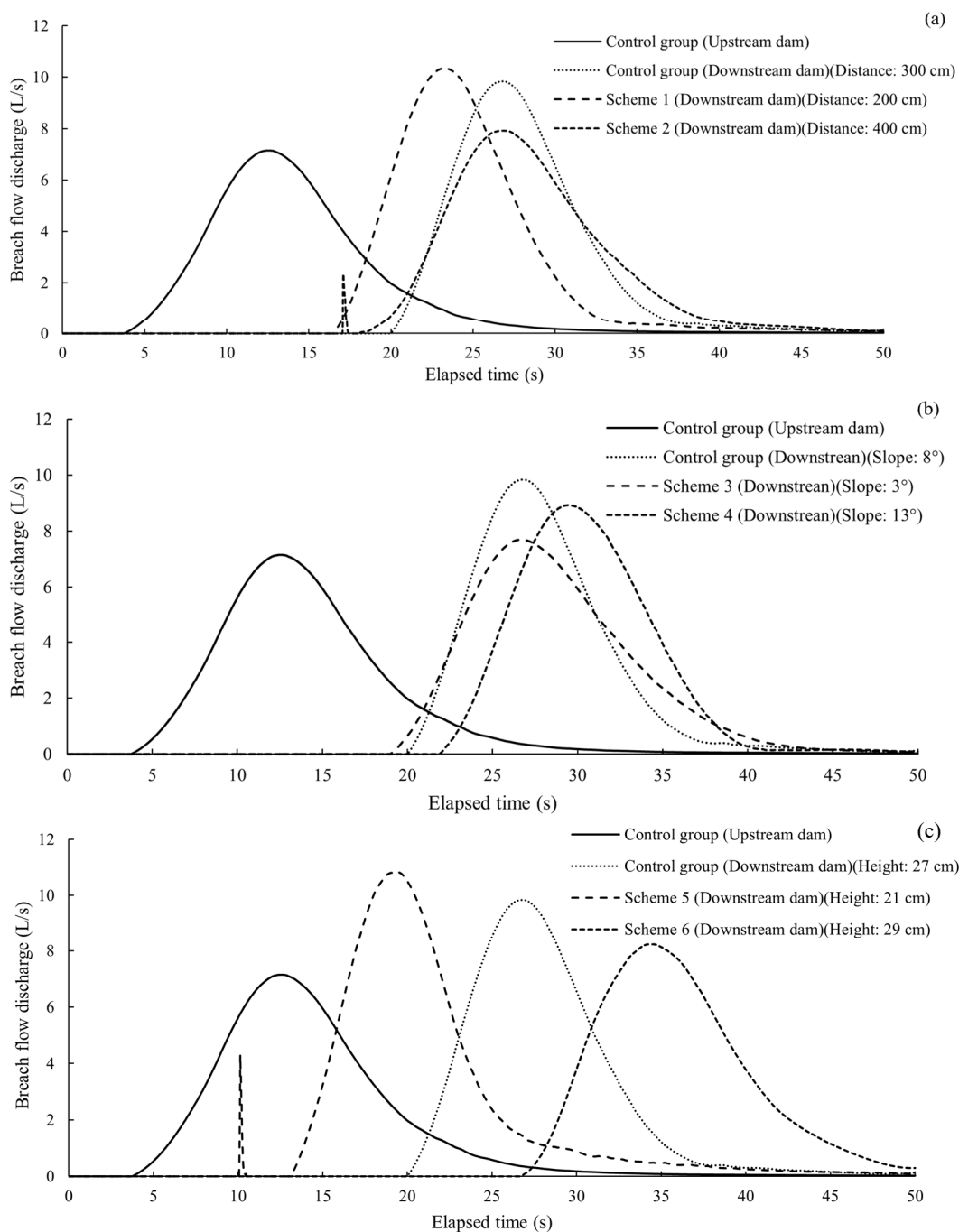


Fig. 10 Sensitivity analyses of cascading dam failure: (a) Different distances between upstream and downstream dams; (b) Different river channel slopes; (c) Different downstream dam heights.

Based on the VOF method, the water-soil interface and the free fluid surface can be traced in the proposed three-dimensional numerical model, and this provides a scientific approach for describing the phenomenon. Secondly, entrainment and deposition of landslide dam material often occur during a landslide dam breaching. In the existing two-dimensional numerical models, it is often assumed that the concentration and

velocity of sediment-carrying flow remain unchanged in the vertical direction, and the exchange of dam material is often judged based on the average physical parameters. On the other hand, in the proposed three-dimensional numerical model, more grids are divided in the vertical direction, thereby ensuring that the entrainment and deposition processes can be calculated based on the hydrodynamic conditions.

4.2 Case study of Xiaogangjian and Lower Xiaogangjian cascading landslide dam failures

To further demonstrate the practicality of the proposed numerical model, the cascading failure case of the Xiaogangjian and Lower Xiaogangjian landslide dams, which were formed because of the 2008 Wenchuan earthquake, has been selected for analyzing the breach process of the two-cascading landslide dams.

4.2.1 Brief introduction

During the Wenchuan earthquake in China, landslides occurred on the right bank of the Mianyuan River, which blocked the river and caused the formation of the Xiaogangjian and Lower Xiaogangjian landslide dams. The locations of the two-cascading landslide dams are illustrated in Fig. 11. The Xiaogangjian landslide dam exhibits a lower left bank and a higher right bank morphology. The elevation of the puerto is 850 m, with the dam height ranging from 70 to 120 m. The lengths of the dam in the cross and longitudinal sections are both approximately 300 m, and the upstream and downstream slope angles are 31° and 25° to 30° , respectively. The maximum storage capacity of the Xiaogangjian dammed lake is approximately $1.025 \times 10^7 \text{ m}^3$. The Lower Xiaogangjian landslide dam locates downstream of the Xiaogangjian landslide dam, with the dam crest elevation approximately at 780 m, and the dam height is about 30 m. The lengths of the dam in the cross and longitudinal sections are both approximately 150 m. The maximum storage capacity of the Lower



Fig. 11 Locations of Xiaogangjian and Lower Xiaogangjian cascading landslide dams.

Xiaogangjian dammed lake is approximately $8.0 \times 10^5 \text{ m}^3$. Since there are significant differences in the dam heights and the storage capacities of the Xiaogangjian and Lower Xiaogangjian landslide dams, once the Xiaogangjian landslide dam fails, it would inevitably trigger subsequent breaching in the Lower Xiaogangjian landslide dam. To mitigate the potential threat to the safety of people's lives and property in the inundation area, a spillway was constructed in the Xiaogangjian landslide dam to drain the water in the dammed lake. The spillway has the inlet elevation of 842.0 m, bottom width of 30 m, and slope ratio of 1:2. After the cascading breach of the Xiaogangjian and Lower Xiaogangjian landslide dams, the final breach depth in the Xiaogangjian landslide dam is approximately 35 m; simultaneously, the Lower Xiaogangjian landslide dam experienced complete failure (Chen et al. 2018).

4.2.2 Development of numerical model

A numerical model for the Xiaogangjian and Lower Xiaogangjian landslide dam failure case has been developed based on the relevant data obtained from on-site investigations, as illustrated in Fig. 12a. The numerical model is constituted by an assemblage of one million discrete grids, with each grid covering an approximate spatial area of 5 m by 5 m. The upstream boundary condition is controlled by a pressure boundary and the downstream boundary condition is set as a free outflow boundary. Two monitoring cross-sections are designated in the numerical model to record the breach flow discharge and the breach morphology evolution processes (Fig. 12b). In the numerical model, the upstream and downstream water levels of the Xiaogangjian landslide dam are set to 847 m and 780 m, respectively. The input parameters for the cascading failure of the Xiaogangjian and Lower Xiaogangjian landslide dams are listed in Table 6.

4.2.3 Comparison of calculated results and measured data

Fig. 13 shows the calculated breach hydrographs of the Xiaogangjian and Lower Xiaogangjian landslide dams and the measured hydrographs from the Hanwang hydrological station, which was 8 km downstream of the Xiaogangjian-lower landslide dam. The calculated results indicate that after the water overtops the spillway of the Xiaogangjian landslide dam, the breach flow increases slowly due to the relatively small flow shear stress. Approximately 130 min after the overtopping of the upstream dam, the

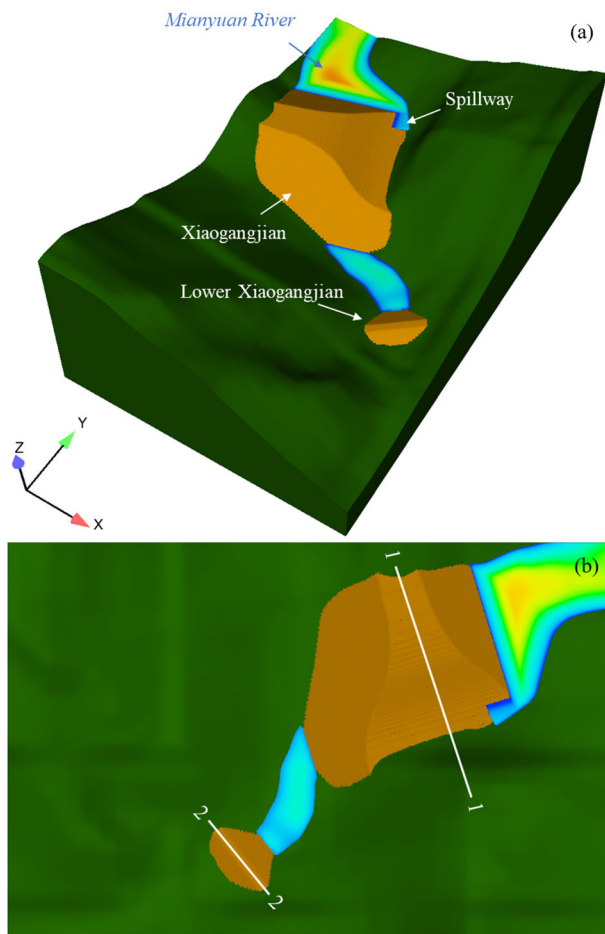


Fig. 12 Numerical model for Xiaogangjian and Lower Xiaogangjian cascading landslide dam failure case: (a) Layout of Xiaogangjian and Lower Xiaogangjian landslide dams in the numerical model, (b) Monitoring sections in the cascading landslide dams (top view).

Table 6 Input parameters for the cascading failures of Xiaogangjian and Lower Xiaogangjian landslide dams

Input parameter	d_{50} (mm)	ρ_s (kg/m ³)	θ_{cr}	α	K	φ (°)
Value	9	2650	0.02	0.018	8	35

breach flow discharge increases rapidly, and reaching the peak flow of 3227.6 m³/s at 170 min after the overtopping of the upstream dam. For the Lower Xiaogangjian landslide dam, the overtopping failure occurs at approximately 133 min after the overtopping of the upstream dam, and reaching the peak breach flow of 3723.5 m³/s at 174 min after the overtopping of the upstream dam. The peak breach flow at the Lower Xiaogangjian landslide dam is 1.15 times of that of the upstream dam. The measured data at the Hanwang hydrological station shows clear signs of flooding at about 175 min after the overtopping of the upstream dam, and reaching the peak flow of 3950 m³/s at 185

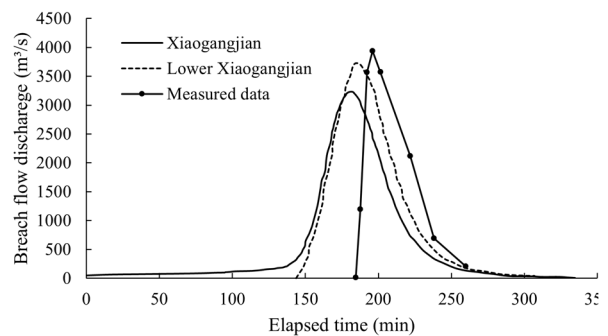


Fig. 13 Comparison of calculated and measured breach hydrographs for the cascading failures of Xiaogangjian and Lower Xiaogangjian landslide dams.

min. Considering the location of the hydrological station and the period for flood routing, the calculated breach hydrograph agrees well with the measured data.

Since the Lower Xiaogangjian landslide dam almost disappear after the cascading failure, the calculated and measured final breach morphologies in Section 2-2 can be considered the same. Therefore, the calculated two-dimensional final breach morphology at Section 1-1 in the Xiaogangjian landslide dam is compared with the on-site monitored data (Chen et al. 2018) (Fig. 14a). Furthermore, the three-dimensional representation of the calculated final breach morphology and the photograph of the actual final breach (Chang and Zhang 2010) are shown in Figs. 14b and 14(c). The information shown in Fig. 16 suggest that the breach at Xiaogangjian was predominantly caused by the unilateral erosion. The calculated and measured final breach elevations are 807.8m and 813.2m, respectively; while the calculated and measured final breach bottom widths are 102.5m and 112.5m, respectively. Regarding the terminal inclinations of the breach’s right bank, the simulated side slope angle is approximately 34.6 degrees, whereas the measured angle is slightly gentler at 30.5 degrees. In general, the results obtained from the numerical simulation replicate those in the breach morphological evolution process of the Xiaogangjian and Lower Xiaogangjian cascading landslide dam failure case, which is an indication of the feasibility of applying the numerical model developed in this study to real-world cases.

Moreover, Table 7 shows the comparison of the calculated and measured key breaching parameters for the cascading failures of the Xiaogangjian and the Lower Xiaogangjian landslide dams. The relative errors of the time to peak and the peak flow are 5.9% and 5.7%, respectively. The relative errors of the final

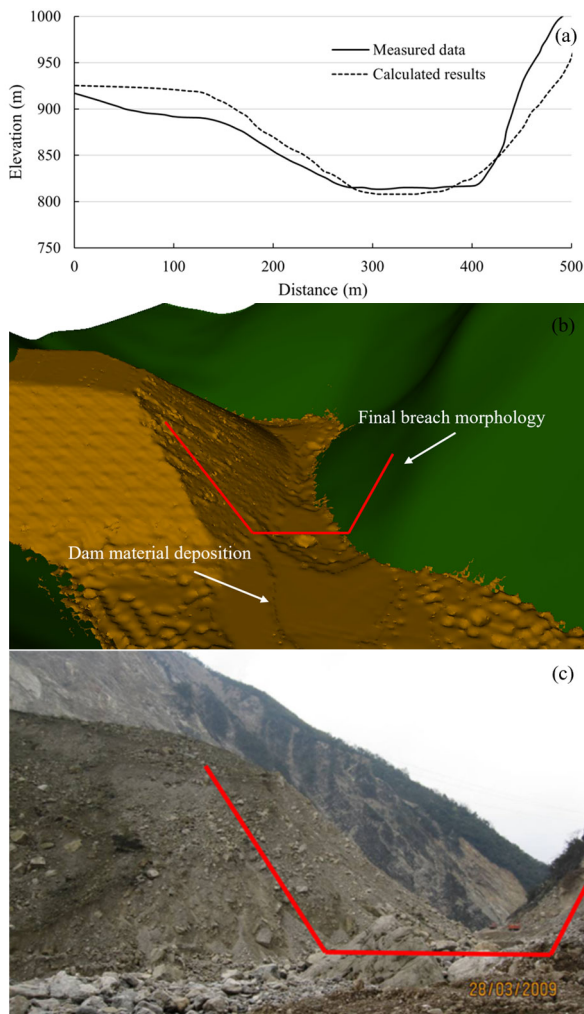


Fig. 14 Comparison of calculated and actual final breach morphologies of Xiaogangjian landslide dam: (a) Comparison of calculated and measured two-dimensional final breach morphologies in Section 1-1; (b) Calculated three-dimensional final breach morphology of Xiaogangjian landslide dam; (c) Actual three-dimensional final breach morphology of Xiaogangjian landslide dam.

breach bottom width and the elevation of the Xiaogangjian landslide dam are 8.9% and 0.7%, respectively. The comparison validates the feasibility of applying the numerical model developed in this study to real-world cases.

Table 7 Comparison of calculated and measured key breaching parameters for the cascading failures of Xiaogangjian and Lower Xiaogangjian landslide dams

Comparison item	Time to peak (min)	Peak flow (m ³ /s)	Final breach bottom width (m)	Final breach bottom elevation (m)
Xiaogangjian	170	3227.6	102.5	807.8
Lower Xiaogangjian	174	3723.5	117.6	756.2
Measured data	185	3950	112.5	813.2
Relative error	5.9%	5.7%	8.9%	0.7%

Note: For the comparison item of "Measured data", time to peak and peak flow are measured in Hanwang hydrological station, and the final breach bottom width and elevation are measured at Xiaogangjian landslide dam after dam breaching.

5 Conclusions

Based on the three-dimensional RANS equations, the RNG *k-ε* turbulence model, the dam material erosion equations, and considering the instability of the breach side slope, a three-dimensional detailed numerical model has been developed in this study. The model can be used to predict a cascading failure process of landslide dams. The rationality of the developed model has been verified using the results of a flume model test and parameter sensitivity analyses. The flood amplification effect of a cascading flood is comprehensively discussed in this paper. The main conclusions of this study are as follows:

(1) A detailed numerical simulation method for a cascading dam failure has been developed. By reproducing the dam-break flow and breach morphology evolution process of cascade dam failures in a physical model test, the practicality and reliability of the numerical model have been verified by comparing the simulated and measured hydro-morphodynamic characteristics during the cascading failure. The numerical model is an effective technical means for simulating cascading landslide dam failures.

(2) From the perspectives of cascading dam distribution, potential energy of river channel, and dam geometric shape, the flood amplification effect of the two-cascading-dam failure has been discussed. Sensitivity analyses of three key parameters, i.e., the distance between the upstream and downstream dams, the river channel slope, and the downstream dam height, have been conducted. The influence of these three key parameters on the flood amplification effect has been revealed. The parameter sensitivity analyses indicate that the peak breach flow increases with shorter distance between the upstream and downstream dams, and the downstream dam height, and increases first and then decreases with steeper river channel slope.

(3) The influence of the surge wave formed by the upstream dam-break flow on the downstream dam

failure process has been discussed. When the surge wave has a large momentum, it can overtop the downstream dam crest and erode the downstream dam body before the water level rises to the downstream dam crest. The quantity of water in the surge wave as it overtops the dam crest and the erosion characteristics of dam material have different degrees of influence on the starting time and breach process of the downstream dam failure.

(4) The cascading failure case of the Xiaogangjian and Lower Xiaogangjian landslide dams has been successfully replicated in the numerical simulations. By comparing the calculated results of the breach hydrographs and the final breach morphology with the observed data, it is found that the relative errors of the key breaching parameters are within the relative errors of $\pm 10\%$. This verifies the practicality of the developed numerical model when applying it to real-world scenarios. The findings in this study contribute significant technical support for the prediction of dam cascading failure risks and the formulation of emergency response plans.

(5) The detailed numerical simulation approach for modeling cascading dam failures continues to confront formidable obstacles pertaining to computational intricacy and suboptimal efficiency. To facilitate real-time assessment of dam breach hazards in future scenarios, the deployment of more progressive methodologies will be imperative to

enhance the computational workflow.

Acknowledgments

This work has been financially supported by the National Natural Science Foundation of China (Grant Nos. U22A20602 and U2040221). We would like to thank MogoEdit (<https://www.mogoedit.com>) for its English editing during the preparation of this manuscript.

Author Contribution

ZHONG Qiming: Material preparation, Data collection, Writing-original draft. CHEN Lingchun: Data analysis, Visualization, Writing-review & editing. MEI Shengyao: Methodology, Formal analysis. SHAN Yibo: Writing-review & editing, Supervision. WU Hao: Writing-review & editing, Supervision. ZHAO Kunpeng: Writing-review & editing, Supervision.

Ethics Declaration

Availability of Data/Materials: All data used in this study are available from the corresponding author upon request.

Conflict of Interest: The authors declare no conflict of interest.

References

- ASCE/EWRI Task Committee on Dam/Levee Breach (2011) Earthen embankment breaching. *J Hydraul Eng* 137: 1549-1564.
[https://doi.org/10.1061/\(ASCE\)HY.1943-7900.0000498](https://doi.org/10.1061/(ASCE)HY.1943-7900.0000498)
- Bagnold RA (1966) An approach to the sediment transport problem from general physics. U.S. Geological Survey Professional Paper 422: 231-291.
- Cao Z, Pender G, Wallis S, et al. (2004) Computational dam-break hydraulics over erodible sediment bed. *J Hydraul Eng* 130: 689-703.
[https://doi.org/10.1061/\(ASCE\)0733-9429\(2004\)130:7\(689\)](https://doi.org/10.1061/(ASCE)0733-9429(2004)130:7(689))
- Cao Z, Yue Z, Pender G (2011) Flood hydraulics due to cascade landslide dam failure. *J Flood Risk Manag* 4: 104-114.
<https://doi.org/10.1111/j.1753-318X.2011.01098.x>
- Chang D, Zhang L (2010) Simulation of the erosion process of landslide dams due to overtopping considering variations in soil erodibility along depth. *Nat Hazard Earth Sys* 10: 933-946.
<https://doi.org/10.5194/nhess-10-933-2010>
- Chen H, Cui P, Zhou GGD, et al. (2014) Experimental study of debris flow caused by domino failures of landslide dams. *Int J Sediment Res* 29: 414-422.
[https://doi.org/10.1016/S1001-6279\(14\)60055-X](https://doi.org/10.1016/S1001-6279(14)60055-X)
- Chen S, Chen Z, Tao R, et al. (2018) Emergency response and back analysis of the failures of earthquake triggered cascade landslide dams on the Mianyuan River, China. *Nat Hazards* Rev 19: 05018005.
[https://doi.org/10.1061/\(ASCE\)NH.1527-6996.0000285](https://doi.org/10.1061/(ASCE)NH.1527-6996.0000285)
- Chen Z, Ma L, Yu S, et al. (2015) Back analysis of the draining process of the Tangjiashan barrier lake. *J Hydraul Eng* 41: 05014011.
[https://doi.org/10.1061/\(ASCE\)HY.1943-7900.0000965](https://doi.org/10.1061/(ASCE)HY.1943-7900.0000965)
- Chien N, Wan Z (1999) *Mechanics of sediment transport*, ASCE Press, Reston, USA.
- Costa JE, Schuster RL (1988) The formation and failure of natural dam. *Geol Soc Am Bull* 100: 1054-1068.
[https://doi.org/10.1130/0016-7606\(1988\)100<1054:TFAFON>2.3.CO;2](https://doi.org/10.1130/0016-7606(1988)100<1054:TFAFON>2.3.CO;2)
- Cui P, Zhu Y, Han Y, et al. (2009) The 12 May Wenchuan earthquake-induced landslide lakes: distribution and preliminary risk evaluation. *Landslides* 7: 209-223.
<https://doi.org/10.1007/s10346-009-0160-9>
- Engelund F, Fredsoe J (1976) A sediment transport model for straight alluvial channels. *Hydrol Res* 7: 293-306.
<https://doi.org/10.2166/nh.1976.0019>
- Fan X, Dufresne A, Subramanian SS, et al. (2020) The formation and impact on landslide dams - State of the art. *Earth Sci Res* 203: 103116.
<https://doi.org/10.1016/j.earscirev.2020.103116>
- Fan X, Juang CH, Wasowski J, et al. (2018) What we have learned from the 2008 Wenchuan Earthquake and its aftermath: A

- decade of research and challenges. *Eng Geol* 241: 25-32.
<https://doi.org/10.1016/j.enggeo.2018.05.004>
- Guan M, Wright NG, Sleigh PA (2014) 2D process-based morphodynamic model for flooding by noncohesive dyke breach. *J Hydraul Eng* 140: 04014022.
[https://doi.org/10.1061/\(ASCE\)HY.1943-7900.0000861](https://doi.org/10.1061/(ASCE)HY.1943-7900.0000861)
- Hirt CW, Nichols BD (1981) Volume of fluid (VOF) method for the dynamics of free boundaries. *J Comput Phys* 39: 201-225.
[https://doi.org/10.1016/0021-9991\(81\)90145-5](https://doi.org/10.1016/0021-9991(81)90145-5)
- Hu W, Li Y, Fan Y, et al. (2022) Flow amplification from cascading landslide dam failures: Insights from flume experiments. *Eng Geol* 297: 106483.
<https://doi.org/10.1016/j.enggeo.2021.106483>
- Kaurav R, Mohapatra PK (2019) Studying the peak discharge through a planar dam breach. *J Hydraul Eng* 145: 06019010.
[https://doi.org/10.1061/\(ASCE\)HY.1943-7900.0001613](https://doi.org/10.1061/(ASCE)HY.1943-7900.0001613)
- Liang C, Abbasi S, Poursahbaz H, et al. (2019) Investigation of flow, erosion, and sedimentation pattern around varied groynes under different hydraulic and geometric conditions: A numerical study. *Water* 11: 235.
<https://doi.org/10.3390/w11020235>
- Marsooli R, Wu W (2015) Three-dimensional numerical modelling of dam-break flows with sediment transport over movable beds. *J Hydraul Eng* 141: 04014066.
[https://doi.org/10.1061/\(ASCE\)HY.1943-7900.0000947](https://doi.org/10.1061/(ASCE)HY.1943-7900.0000947)
- Mastbergen DR, Berg J, (2003) Breaching in fine sands and the generation of sustained turbidity currents in submarine canyons. *Sedimentology* 50: 625-637.
<https://doi.org/10.1046/j.1365-3091.2003.00554.x>
- Mei S, Chen S, Zhong Q, et al. (2022) Detailed numerical modeling for breach hydrograph and morphology evolution during landslide dam breaching. *Landslides* 19: 2925-2949.
<https://doi.org/10.1007/s10346-022-01952-1>
- Mei S, Zhong Q, Yang M, et al. (2023) Overtopping-induced breaching process of concrete-faced rockfill dam: A case study of Upper Taum Sauk Dam. *Eng Fail Anal* 144: 106982.
<https://doi.org/10.1016/j.engfailanal.2022.106982>
- Meyer-Peter E, Muller R (1948) Formulas for bedload transport. *Process of Congress IAHR* 6(2): 39-64.
- Movahedi A, Kavianpour MR, Yamini OA (2018) Evaluation and modeling scouring and sedimentation around downstream of large dams. *Environ Earth Sci* 77: 320.
<https://doi.org/10.1007/s12665-018-7487-2>
- Nielsen P (1992) Coastal bottom boundary layers and sediment transport. *Advanced Series on Ocean Engineering*, Volume 4, World Scientific, Singapore.
- Niu Z, Xu W, Li N, et al. (2012) Experimental investigation of the failure of cascade landslide dams. *J Hydrodyn* 24: 430-441.
[https://doi.org/10.1016/S1001-6058\(11\)60264-3](https://doi.org/10.1016/S1001-6058(11)60264-3)
- Roseberry JC, Schmeckle MW, Furbish DJ (2012). A probabilistic description of the bed load sediment flux: 2. Particle activity and motions. *J Geophys Res-Earth* 117: F03032.
<https://doi.org/10.1029/2012JF002353>
- Samma H, Khosrojerdi A, Rostam-Abadi M, et al. (2020) Numerical simulation of scour and flow field over movable bed induced by a submerged wall jet. *J Hydroinform* 22: 385-401.
<https://doi.org/10.2166/hydro.2020.091>
- Shen D, Shi Z, Peng M, et al. (2020) Longevity analysis of landslide dams. *Landslides* 17: 1797-1821.
<https://doi.org/10.1007/s10346-020-01386-7>
- Shi Z, Guana SG, Peng M, et al. (2015) Cascading breaching of the Tangjiashan landslide dam and two smaller downstream landslide dams. *Eng Geol* 193: 445-458.
<https://doi.org/10.1016/j.enggeo.2015.05.021>
- Soulsby R (1997) Chapter 9: Bedload transport. *Dynamics of Marine Sand*. Thomas Telford Publications, London.
- Takayama S, Fujimoto M, Satofuka Y (2021) Amplification of flood discharge caused by the cascading failure of landslide dams. *Int J Sediment Res* 36: 430-438.
<https://doi.org/10.1016/j.ijsrc.2020.10.007>
- Van Rijn L (1984) Sediment transport, Part I: bed load transport. *J Hydraul Eng* 110: 1431-1456.
[https://doi.org/10.1061/\(ASCE\)0733-9429\(1984\)110:10\(1431\)](https://doi.org/10.1061/(ASCE)0733-9429(1984)110:10(1431))
- Yakhot V, Orszag SA, Thangam S, et al. (1992) Development of turbulence models for shear flows by a double expansion technique. *Phys Fluids* 4: 1510-1520.
<https://doi.org/10.1063/1.858424>
- Wu H, Shi A, Ni W, et al. (2024) Numerical simulation on potential landslide-induced wave hazards by a novel hybrid method. *Eng Geol* 331: 107429.
<https://doi.org/10.1016/j.enggeo.2024.107429>
- Yang Q, Guan M, Peng Y, et al. (2020) Numerical investigation of flash flood dynamics due to cascading failures of natural landslide dams. *Eng Geol* 276: 105765.
<https://doi.org/10.1016/j.enggeo.2020.105765>
- Zheng H, Shi Z, Peng M, et al. (2022) Amplification effect of cascading breach discharge of landslide dams. *Landslides* 19: 573-587.
<https://doi.org/10.1007/s10346-021-01816-0>
- Zhong Q, Wang L, Chen S, et al. (2021) Breaches of embankment and landslide dams - State of the art review. *Earth-Sci Rev* 216: 103597.
<https://doi.org/10.1016/j.earscirev.2021.103597>
- Zhong Q, Wu W, Chen S, et al. (2016) Comparison of simplified physically based dam breach models. *Nat Hazards* 84: 1385-1418.
<https://doi.org/10.1007/s11069-016-2492-9>
- Zhou GGD, Lu X, Xie Y, et al. (2022) Mechanisms of the non-uniform breach morphology evolution of landslide dams composed of unconsolidated sediments during overtopping failure. *J Geophys Res-Earth* 127: e2022JF006664.
<https://doi.org/10.1029/2022JF006664>
- Zhou GGD, Cui P, Chen H, et al. 2013. Experimental study on cascading landslide dam failures by upstream flows. *Landslides* 10: 633-643.
<https://doi.org/10.1007/s10346-012-0352-6>
- Zhou GGD, Cui P, Zhu X, et al. (2015) A preliminary study of the failure mechanisms of cascading landslide dams. *Int J Sediment Res* 30: 223-234.
<https://doi.org/10.1016/j.ijsrc.2014.09.003>
- Zhu Y, Peng M, Cai S, et al. (2021) Risk-based warning decision making of cascade breaching of the Tangjiashan landslide dam and two smaller downstream landslide dams. *Front Earth Sc-Switz* 9: 648919.
<https://doi.org/10.3389/feart.2021.648919>